nature microbiology

LETTERS

https://doi.org/10.1038/s41564-018-0128-4

Coccolithovirus facilitation of carbon export in the North Atlantic

Christien P. Laber[1], Jonathan E. Hunter[2], Filipa Carvalho[1,8], James R. Collins[2], Elias J. Hunter[1], Brittany M. Schieler[1], Emmanuel Boss[3], Kuldeep More[4], Miguel Frada[5,9], Kimberlee Thamatrakoln[1], Christopher M. Brown[1], Liti Haramaty[1], Justin Ossolinski[2], Helen Fredricks[2], Jozef I. Nissimov[1], Rebecca Vandzura[1,10], Uri Sheyn[5], Yoav Lehahn[5,11], Robert J. Chant[1], Ana M. Martins[6], Marco J. L. Coolen[4], Assaf Vardi[5], Giacomo R. DiTullio[7], Benjamin A. S. Van Mooy[2] and Kay D. Bidle[1]*

Marine phytoplankton account for approximately half of global primary productivity[1], making their fate an important driver of the marine carbon cycle. Viruses are thought to recycle more than one-quarter of oceanic photosynthetically fixed organic carbon[2], which can stimulate nutrient regeneration, primary production and upper ocean respiration[2] via lytic infection and the 'virus shunt'. Ultimately, this limits the trophic transfer of carbon and energy to both higher food webs and the deep ocean[2]. Using imagery taken by the Moderate Resolution Imaging Spectroradiometer (MODIS) onboard the Aqua satellite, along with a suite of diagnostic lipid- and gene-based molecular biomarkers, in situ optical sensors and sediment traps, we show that *Coccolithovirus* infections of mesoscale (~100 km) *Emiliania huxleyi* blooms in the North Atlantic are coupled with particle aggregation, high zooplankton grazing and greater downward vertical fluxes of both particulate organic and particulate inorganic carbon from the upper mixed layer. Our analyses captured blooms in different phases of infection (early, late and post) and revealed the highest export flux in 'early-infected blooms' with sinking particles being disproportionately enriched with infected cells and subsequently remineralized at depth in the mesopelagic. Our findings reveal viral infection as a previously unrecognized ecosystem process enhancing biological pump efficiency.

Coccolithophores—calcified photosynthetic protists—account for ~20% of marine primary productivity[3], 12% ($0.2\,Gt\,yr^{-1}$) of global $CaCO_3$ export flux and half of the $CaCO_3$ reservoirs reaching deep sea sediments[4]. The most abundant and globally distributed coccolithophore *Emiliania huxleyi* forms massive blooms in the oceans that can exceed $10^5\,km^2$, with cell densities reaching $10^5\,cells\,ml^{-1}$ (ref. [5]). The termination of dense coastal and open-ocean North Atlantic blooms of *E. huxleyi*, which can last over a period of days to weeks, is commonly attributed to infection by double-stranded-DNA-containing coccolithoviruses (EhVs)[6–8]. The interaction between *E. huxleyi* and EhVs is mediated by a lipid-based, co-evolutionary arms race centred around the rewiring of host lipid metabolism, glycosphingolipid (GSL) production and the activation and recruitment of the host's oxidative stress, autophagy and programmed cell death pathways—a process that takes between 72 and 96 h[9–12]. This mechanistic insight has led to the development of functional biomarkers[7,10,13], which can now be used to diagnose the level of active infection in natural oceanic populations and quantitatively assess its ecosystem and biogeochemical impacts—a capability that has been lacking in virus ecology.

A unique suite of structurally distinct polar lipids—GSLs and betaine-like lipids (BLLs)—represent distinct functional aspects of the *E. huxleyi*–EhV infection process[7,10,13,14]. Host-specific GSLs (hGSLs) are both abundant and constitutively produced in *E. huxleyi* cells, providing more taxonomic resolution than the 19'-hexanoyloxyfucoxanthin pigment. Viral GSLs (vGSLs) are critical to and diagnostic of successful infection[10,12], triggering the production of reactive oxygen species, autophagy, programmed cell death and eventual lysis of *E. huxleyi* cells[9–11]. EhV infection also specifically triggers an exponential increase in BLL(22:6/22:6), which becomes the major BLL species in infected cells[14]. At the same time, sialic acid GSLs (sGSLs) provide a diagnostic of population susceptibility to EhV infection, having only been detected in susceptible *E. huxleyi* strains[13].

The manner in which phytoplankton die ultimately determines the flow of photosynthetically fixed organic matter (and associated elements) and relative coupling through three main ecosystem pathways— transfer to higher trophic levels via grazing, recycling through the microbial loop and downward export via sinking—each of which has distinct biogeochemical consequences[15]. Pairing the aforementioned diagnostic biomarkers with high-resolution in situ measurements from observational sensing platforms stands to elucidate broader ecosystem and biogeochemical consequences of infection. The impact of virus infection on optical backscatter (B_b), chlorophyll *a* (Chl *a*), dissolved oxygen and chromophoric dissolved organic matter (CDOM) remain unexplored as possible signals and indicators of acute viral infection events. EhV infection is thought to alter B_b during infection as the host sheds and produces free coccoliths, while leaking and lysing cells may release dissolved organic matter as respiratory substrates and components of CDOM[16]. At the

[1]Department of Marine and Coastal Sciences, Rutgers University, New Brunswick, NJ, USA. [2]Department of Chemistry and Geochemistry, Woods Hole Oceanographic Institution, Woods Hole, MA, USA. [3]School of Marine Sciences, University of Maine, Walpole, ME, USA. [4]Western Australian Organic and Isotope Geochemistry Center, Department of Chemistry, Curtin University, Bentley, WA, Australia. [5]Department of Plant and Environmental Sciences, Weizmann Institute of Science, Rehovot, Israel. [6]Department of Oceanography and Fisheries, University of the Azores, Faial, Azores, Portugal. [7]Grice Marine Laboratory, College of Charleston, Charleston, SC, USA. Present address: [8]National Oceanography Centre, Southampton, United Kingdom. [9]The Interuniversity Institute for Marine Sciences—Eilat, Eilat, Israel. [10]College of Earth, Ocean and Environment, University of Delaware, Newark, DE, USA. [11]Department of Marine Geosciences, University of Haifa, Haifa, Israel. *e-mail: bidle@marine.rutgers.edu

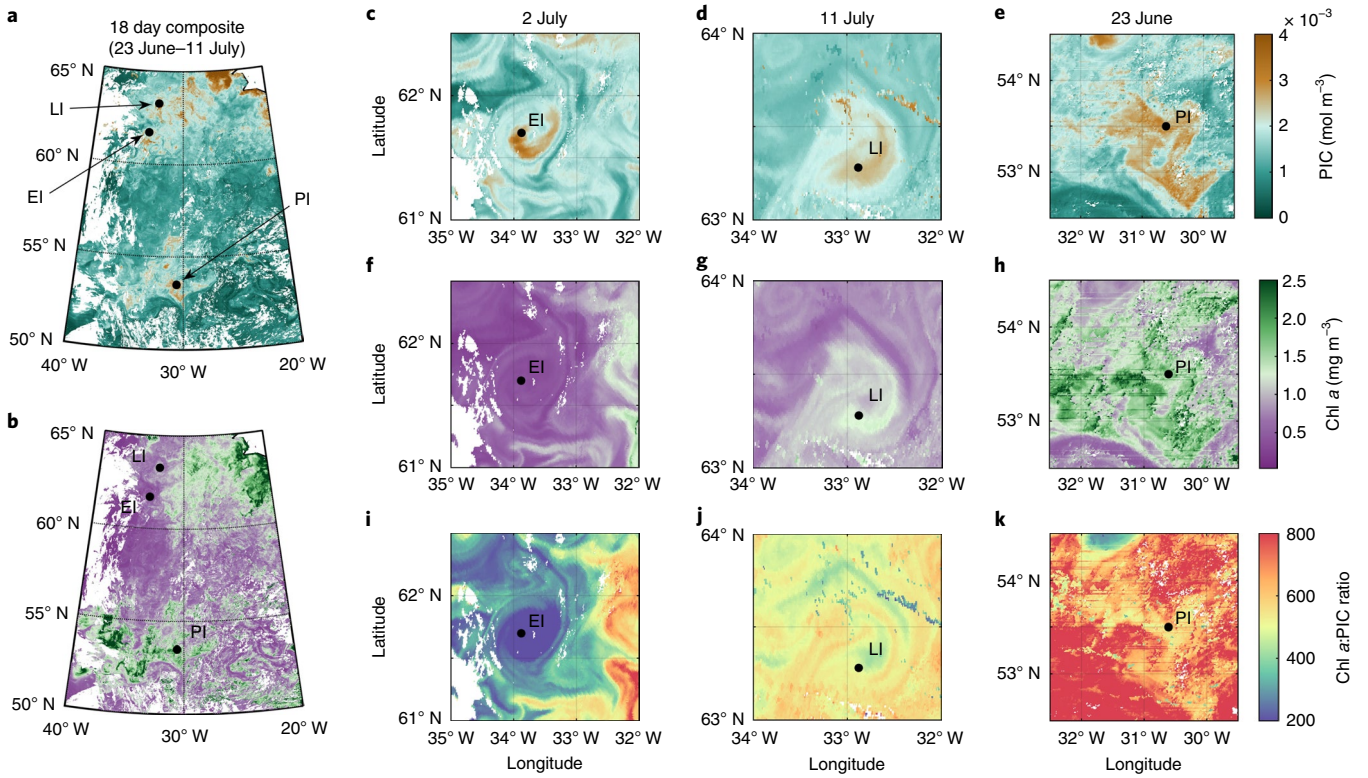

Fig. 1 | MODIS/Aqua (1 km resolution)-derived near-surface PIC and Chl *a* concentration images of water mass features containing *E. huxleyi* blooms in the North Atlantic. a,**b**, Location and overview of PIC (**a**) and Chl *a* (**b**) at water masses sampled in the North Atlantic. EI populations were occupied from 30 June to 5 July and again from 7–11 July (EI_R). LI populations were occupied on 6 July and 12 July, with regular profiling float measurements taken continuously between occupations. PI populations were occupied from 23–27 June. Note that the PIC and Chl *a* concentration scales are on the far right. **c**–**e**, Satellite PIC measurements showed elevated PIC at each station during occupation. **f**–**h**, In contrast, Chl *a* showed more variability between stations; the lowest concentration was at EI and the highest was at PI. **i**–**k**, The resulting Chl *a*:PIC ratios associated with resident populations were quite different at each water mass (low ratios at EI, intermediate at LI and high at PI), consistent with differences in physiological state, phytoplankton composition or photoacclimation. For **a** and **b**, 1 km^2 pixels are from a maximum average of 18 d and a minimum of 1 d depending on cloud cover. For **c**–**k**, 1 km^2 pixels are from single-day observations (one observation per day).

same time, EhV infection enhances cellular production of transparent exopolymer particles (TEP)—sticky, particle-aggregating polysaccharide matrices[7,17]—and can trigger preferential grazing responses[18]. The particle production associated with these pathways (aggregates and faecal pellets from grazers), together with ballasting provided by $CaCO_3$ coccoliths (density (ρ) = 2.8 g cm^{-3}), provide mechanisms[19,20] by which viruses may contribute to downward export instead of fuelling the futile carbon cycle through rapid upper water column remineralization via the microbial loop[21].

We tested the hypothesis that *Coccolithovirus* infection of *E. huxleyi* facilitates downward vertical flux of both particulate organic carbon (POC) and particulate inorganic carbon (PIC) during the North Atlantic Viral Infection of Coccolithophores Expedition (NA-VICE) (see Methods; Fig. 1). Host–virus interactions and associated ecosystem dynamics were interrogated over 4–5 d using a Lagrangian mode sampling strategy within and below the mixed layer (down to 300 m) and through a combination of water samples obtained via traditional conductivity–temperature–depth (CTD) casts and deployments of both surface-tethered sediment traps and vertically migrating in situ optical profilers (see Methods). The timing of occupation and field sampling strategies were specifically designed to take advantage of the well-documented ~4 d infection window and to interrogate its potential impact on ecosystem dynamics and the potential export of biomineral-rich particles with high sinking rates[7,10,11]. Our postcruise analyses identified three physically and biologically distinct water features containing *E. huxleyi* blooms at different phases of EhV infection—early infection (EI), late infection (LI) and postinfection (PI) (see Methods and details below for how these phases were diagnosed). EI and LI populations were within distinct anticyclonic mesoscale eddy features with sampling efforts following the clockwise rotation pattern; the PI water mass coherently migrated south during sampling and began mixing with a fresher water mass at the end of our occupation (Supplementary Figs. 1 and 2). A second visit to EI (EI_R), two days later, followed a more central trajectory within the eddy.

Remote-sensing analysis of these three features showed elevated PIC signals indicative of coccolithophore blooms, but the satellite-derived Chl *a* concentration varied widely; Chl *a* was lowest at EI, intermediate at LI and relatively high at PI (Fig. 1). This made for disparate Chl *a*:PIC signature ratios (that is, low at EI, intermediate at LI and high at PI)—features consistent with differences in physiological state, phytoplankton composition and/or photoacclimation. Meanwhile, *E. huxleyi* cell densities ranged from ~1–4 × 10^3 cells ml^{-1} at EI and EI_R, similar to other large-scale *E. huxleyi* blooms reported in the North Atlantic and elsewhere (Supplementary Fig. 3). Depth-integrated *E. huxleyi* cell abundances to 150 m revealed larger cell inventories at EI and EI_R (7 × 10^5 and 8 × 10^5 cells m^{-2}, respectively) than LI and PI (5 × 10^5 and 2 × 10^5 cells m^{-2}, respectively).

We deployed vertical profiling floats equipped with Bio-Optical Sensor System mini packages (see Methods) to characterize the dynamic in situ biological and chemical signals associated with different stages of EhV infection. Observations spanning the euphotic

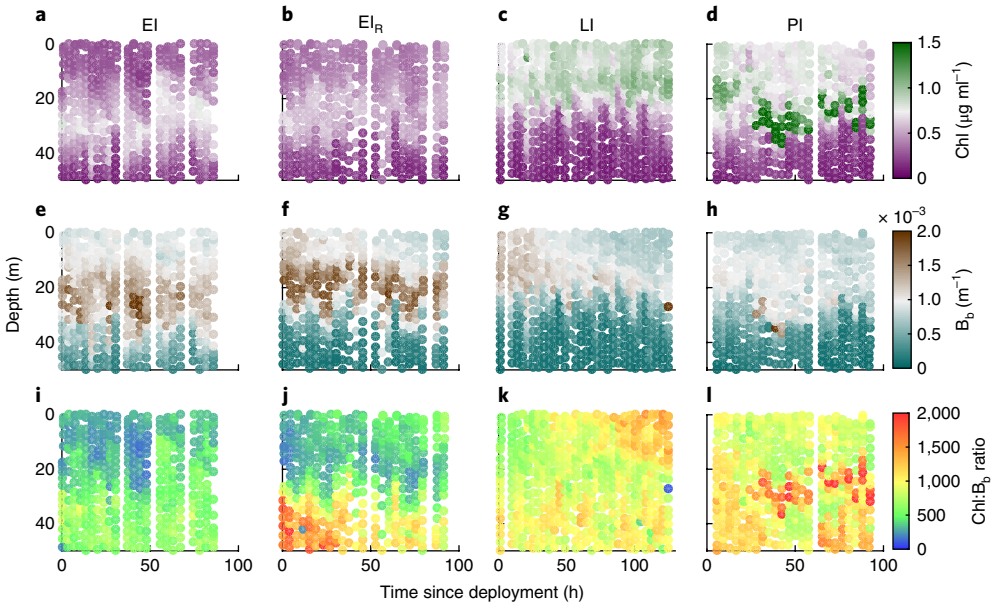

Fig. 2 | Natural populations at different stages of EhV infection have distinct in situ optical properties. a–d, Relatively low Chl fluorescence is observed in the water column at EI (**a**) and EI$_R$ (**b**) compared with the rapidly increasing Chl at LI (**c**) and high signal observed at PI (**d**). **e–h**, For B_b (700 nm) the opposite trend is observed, with the highest levels at EI (**e**) EI$_R$ (**f**), a rapid decrease over the observation period at LI (**g**) and low levels at PI (**h**). **i–l**, These patterns drive an increasing Chl:B_b ratio signal from EI (**i**) and EI$_R$ (**j**), to LI (**k**), and finally PI (**l**) populations, similar to the satellite Chl *a*:PIC ratio observations (Fig. 1i–k). For each data point, $n = 1$ technical replicate.

zone depths generally affirmed the satellite Chl *a* data, revealing relatively low Chl *a* at the EI and EI$_R$ deployments, increasing through the deployment at LI and highest at PI (Fig. 2a–d). B_b measurements showed an opposite trend (Fig. 2e–h), influenced by the abundances of coccolithophores and shed coccoliths (Supplementary Figs. 4 and 5); they were highest at EI and EI$_R$, decreasing rapidly during LI, and reaching relatively low levels at PI. Notably, respective in situ Chl *a*:B_b ratios also corroborated and complemented the satellite-derived Chl *a*:PIC with a roughly fourfold difference in Chl *a*:B_b between the EI and PI states (Fig. 2i–l). We suggest that the lower Chl *a*:B_b ratios associated with the EI and EI$_R$ communities were due to the abundance of coccolithophores and that this is a characteristic signature of an intense *E. huxleyi* bloom. Even though pigment data suggest that *E. huxleyi* and closely related haptophytes contributed 50–60% of the total Chl *a* signal on average (Supplementary Fig. 6), the high scattering characteristics of coccoliths provided a more robust influence on the Chl *a*:B_b ratio than the other eukaryotic phytoplankton groups or the numerically dominant picocyanobacteria (Supplementary Fig. 4).

Depth-integrated measurements of different GSL parameters (that is, sGSL and vGSL inventories, and vGSL:hGSL and vGSL:sGSL ratios) revealed that *E. huxleyi* were at different stages of infection (Fig. 3a–d). These diagnostics are grounded by fine-scale observations of the parameters at high temporal resolution in well-characterized events of EhV-induced bloom termination in both laboratory and mesocosm settings[7,10,13]. Both EI and EI$_R$ exhibited low vGSL:sGSL and vGSL:hGSL concentration ratios, indicating a resident *E. huxleyi* population that was highly sensitive (represented by high sGSL inventories) and undergoing EI (as indicated by the low, yet detectable inventories of vGSLs). PI had a significantly lower concentration of sGSLs in the upper 150 m compared with EI and EI$_R$, indicating a greatly reduced population of sensitive cells. It also had the highest vGSL:sGSL and vGSL:hGSL ratios, consistent with a sensitive *E. huxleyi* population that had been terminated by a mature EhV infection. The LI population had intermediate hGSL, sGSL and vGSL characteristics, consistent with cells transitioning between infected and PI stages.

Independent, DNA-based quantitative polymerase chain reaction (qPCR) analysis corroborated the lipid-based observations of EhV infection (Fig. 3e–g). Importantly, our GSL and qPCR analyses were based on independent macromolecular pools and extracted from biomass collected onto 0.8 μm pore-size filters, thereby reflecting EhVs associated with (and replicating within) *E. huxleyi* cells. Cytochrome oxidase c subunit 1(COI)-based *E. huxleyi* numbers ranged from 9×10^1 to 8×10^6 cells l^{-1}, while major capsid protein (MCP)-based EhV abundances associated with *E. huxleyi* cells ranged from 6×10^3 to 9×10^8 virions l^{-1}. The highest *E. huxleyi* COI copy numbers were at EI and EI$_R$ (Fig. 3e), consistent with the high *E. huxleyi* abundances measured via flow cytometry. CHEMTAX pigment analyses corroborated that the contribution of *E. huxleyi* to total phytoplankton Chl *a* biomass was higher during the EI stages (20%) than LI (12%) and PI (15%), while dinoflagellates, prasinophytes, chlorophytes and diatoms displayed increasing contributions to the communities at LI and PI (Supplementary Fig. 6). Total cell-associated MCP copy numbers were similar across stations (Fig. 3f), which appeared to be largely driven by host biomass. MCP:COI ratios were highest in the PI population indicative of more infected cells, with relatively low COI-based host abundances and a more advanced stage of lytic infection (Fig. 3g). *E. huxleyi* cell mortality, taken as operationally dead cells with compromised membranes, was greatly elevated at PI (85%) and LI (66%) compared with EI (42%) and EI$_R$ (33%), further supporting discrete stages of infection (Supplementary Fig. 7).

Sediment trap measurements in conjunction with a 'spike' transformation of the profiling float B_b profiles[19] quantified particle flux dynamics via the removal of POC and PIC from the surface ocean in relation to EhV infection signatures. Elevated POC and PIC fluxes (maxima of 109 and 249 mg C m^{-2} d^{-1} at 50 m, respectively) corresponded to the EI and EI$_R$ populations during NA-VICE[22], far exceeding flux rates at PI (59 and 7 mg C m^{-2} d^{-1}, respectively) and other stations without *E. huxleyi* blooms. The B_b spike transformation analysis, previously used to discern sinking aggregated phytoplankton and detrital matter[19], corroborated sediment trap flux measurements (Fig. 4a and Supplementary Fig. 8). Higher spike

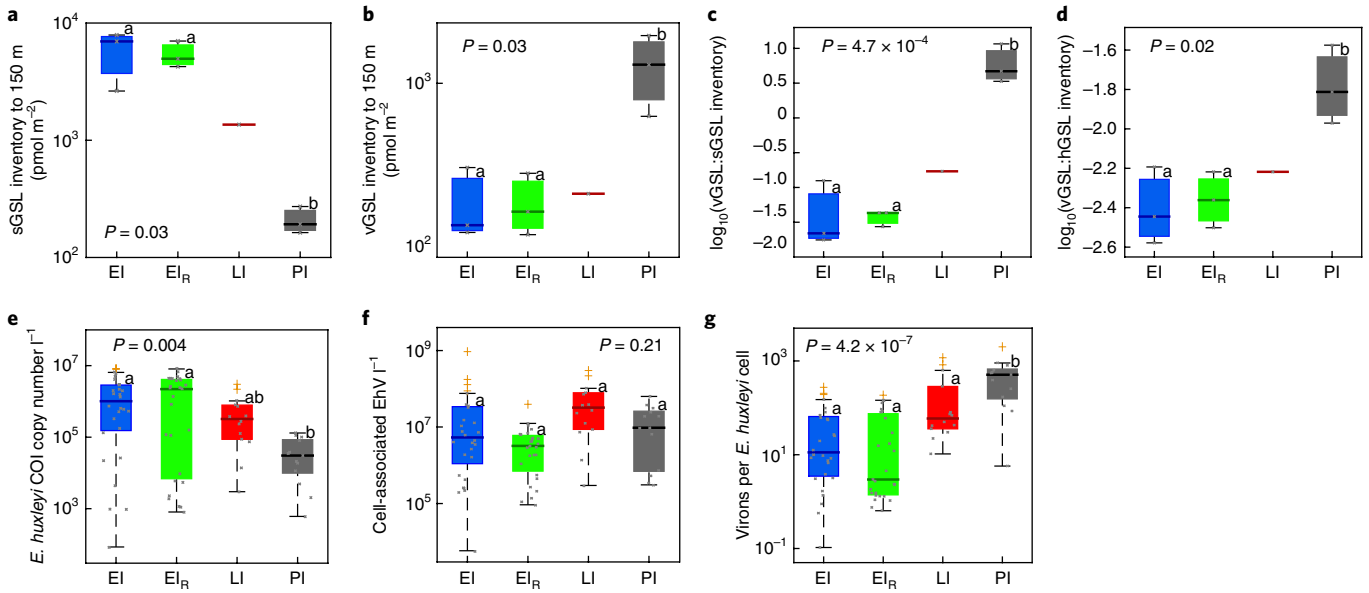

Fig. 3 | Diagnosis of virus infection using lipid- and DNA-based biomolecular proxies. a–d, Box and whisker plots of sGSL (**a**) and vGSL (**b**) inventories (down to 150 m; blue, EI; green, EI$_R$; red, LI; grey, PI) and vGSL:sGSL (**c**) and vGSL:hGSL (**d**) inventory ratios at each station reveal distinct stages of infection. **e**, Corresponding COI-based qPCR results reveal that *E. huxleyi* abundance was higher for EI and EI$_R$ than PI. **f**, The MCP gene copy number, representing EhV abundance, was similar across stations. **g**, EhVs per *E. huxleyi* cell, expressed as the ratio of MCP:COI gene copy numbers, were highest at PI. For all plots, upper and lower box bounds denote 25 and 75% quantiles around the median (thick line). Vertical capped lines indicate maximum and minimum data values. Outliers are indicated with a + sign. The letters above the boxes denote statistically different groups based on ANOVA. For **a–d**, EI, $n=3$; EI$_R$, $n=3$; LI, $n=1$; PI, $n=3$ station replicates; LI was excluded from the statistical analysis, given the lack of replicate inventories. Grey crosses indicate individual data points. For **e–g**, EI, $n=28$; EI$_R$, $n=28$; LI, $n=14$; PI, $n=13$ station replicates. Pairwise comparisons for EI:EI$_R$, EI:PI and EI$_R$:PI in **a–d** gave the *P* values 0.99, 0.035 and 0.048 (**a**) 0.99, 0.044 and 0.045 (**b**) 0.99, 6.5×10^{-4} and 6.7×10^{-4} (**c**), and 0.99, 0.022 and 0.031 (**d**). Pairwise comparisons for EI:EI$_R$, EI:LI, EI:PI, EI$_R$:LI, EI$_R$:PI and LI:PI in **e–g** gave the *P* values 0.99, 0.16, 0.02, 0.10, 0.01 and 0.85 (**e**), 0.31, 0.99, 0.70, 0.34, 0.98 and 0.65 (**f**), and 0.99, 0.12, 1.82×10^{-6}, 0.089, 1.19×10^{-6} and 0.020 (**g**).

signals were observed below 50 m at EI and EI$_R$ compared with LI and PI, consistent with greater aggregate sinking during EI and dissipating following virus-induced termination. Notably, the EI and EI$_R$ populations were associated with some of the lowest recorded POC:PIC export ratios (2.3 and 4.3 at 50 m, respectively) in the North Atlantic, driven by the extremely high fluxes of PIC[22].

Vertical inventories of dissolved oxygen measured from in situ optical profilers provided a platform to investigate the biogeochemical fate and rates of carbon remineralization (C_{remin}) of the POC exported below the mixed layer (>50 m; see Methods). We observed distinct oxygen minimum layers below the mixed layer at each station, which were accompanied by steady decreases in submixed layer water column dissolved oxygen concentrations for EI, EI$_R$ and LI populations (Supplementary Fig. 9). EI and EI$_R$ had up to ninefold higher C_{remin} than LI, with C_{remin} maxima in the mesopelagic between 125 and 200 m (Fig. 4b) and similar depth-integrated results comparable to direct observations (Supplementary Table 1). C_{remin} calculations at PI were not possible due to the mixing of water masses. Elevated CDOM did not coincide with the high C_{remin} rates (Supplementary Fig. 10), arguing against it supporting respiration in the water column; other forms of dissolved organic matter were not accounted for in our measurements. Our findings link the enhanced flux rates at EI and EI$_R$ with greatly elevated C_{remin} due to the respiration of transient sinking particles in the mesopelagic[22].

Lipidomics of sinking particles collected in net traps directly supported EhV infection as a contributing mechanism to enhanced export. We observed significantly higher BLL(22:6/22:6)-to-BLL(18:1/22:6) ratios[14] in sediment trap material than in water column samples from both above and below the mixed layer (Fig. 4c and Supplementary Fig. 11), indicating a higher proportion of infected cells in sinking particles. No significant difference was observed for water column samples in or below the mixed layer. Statistically significant correlations between sGSLs and PIC flux confirmed that susceptible cells dominated the coccolith/coccolithophore export (Fig. 4d and Supplementary Table 2); PIC fluxes did not correlate with hGSLs—a marker for all *E. huxleyi* cells. The disproportional enrichment of infected cells in exported material provides strong evidence for EhV-induced carbon flux. Notably, downwelling-induced vertical transport did not appear to account for observed fluxes of infected particles[23], as it would serve to homogenize rather than decouple the observed lipid signals. Indeed, downwelling-driven Chl injection into deep water was not observed in our data. In fact, expression profiling of genes upregulated during infection also showed that active infection at EI and EI$_R$ occurred below the pycnocline, with the degree of infection correlating with depth[24].

We quantitatively addressed the geographic source of trap material using the available acoustic Doppler current profiler (ADCP) data from the research vessel *(RV) Knorr* along with the transit trajectories of the surface-tethered traps (at 50, 150 and 300 m; see Methods). Lagrangian dispersion simulations indicated that the footprint containing 99% of particles from the 50, 150 and 300 m traps originated in circles of radius 2, 5 and 7 km, respectively, at EI, EI$_R$ and LI (Fig. 4e,f). This suggests that the source material for particles transiting to sediment traps was probably derived from the infected bloom above and within the local water mass boundaries, as opposed to lateral advection from adjacent water masses. Furthermore, the respective BLL and sGSL:hGSL ratios were statistically indistinguishable with trap depth, indicating that the dominant signal derived from the same, rapidly sinking source material rather than a separate population that had been infected before our occupation.

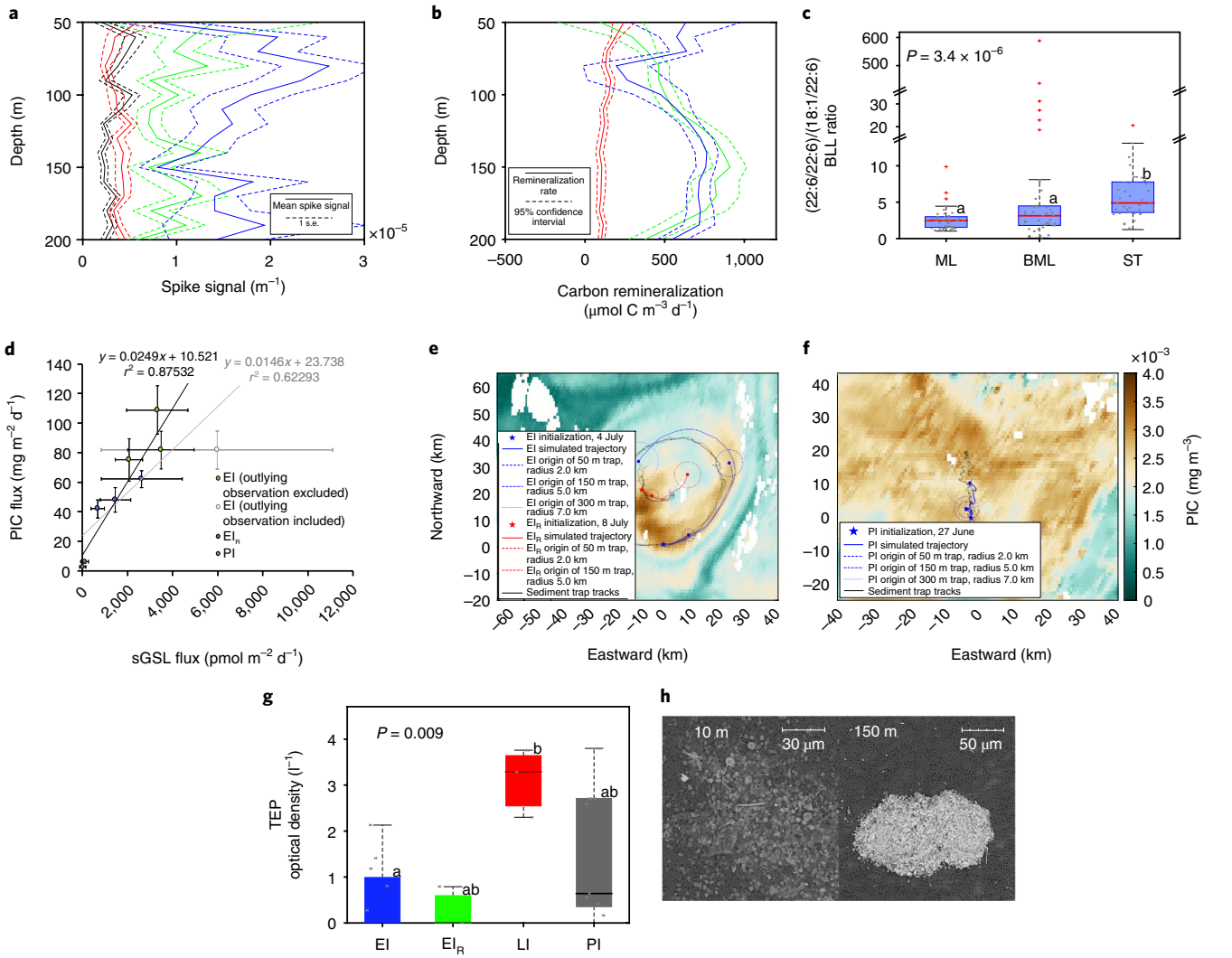

Fig. 4 | Active EhV infection triggers TEP-facilitated aggregation, POC export and remineralization in the mesopelagic. a, B_b spike signals reveal elevated particle aggregates at EI and EI$_R$ (blue and green, respectively) below the euphotic zone compared with LI and PI (red and black, respectively). Centroids indicate the mean spike signal for 10 m bins over an entire float deployment. Dotted lines indicate ±1 s.e. **b**, Particle dynamics at EI and EI$_R$ were accompanied by high carbon remineralization rates in the mesopelagic. Dotted lines indicate 95% confidence intervals from linear regression. In **a** and **b**, for EI, EI$_R$, LI and PI, $n = 25$, 25, 31 and 24, respectively. **c**,**d**, Susceptible EhV-infected cells were preferentially exported. **c**, BLL(22:6/22:6)/(18:1/22:6) ratios for suspended biomass in the mixed layer (ML; down to 30 m), below the mixed layer (BML) and in sediment traps (ST; positioned at 50, 150 and 300 m). Kruskal–Wallis ANOVA showed significantly higher ratios in the ST material. The letters above the boxes denote statistically different groups. Pairwise comparisons for ML:BML, ML:ST and BML:ST gave P values of 0.14, 1.93×10^{-6} and 0.004, respectively. For ML, BML and ST, $n = 41$, 43 and 37 environmental replicates, respectively. **d**, Elevated PIC sinking flux was accompanied by increased sGSL sinking flux in the same sediment trap material. The error bars signify 1 s.d. around the mean (centroid). **e**,**f**, Modelled geographic origins of sinking particles. MODIS/Aqua PIC images on 3 July (**e**) and 23 June (**f**). Tracks of deployed sediment traps are shown in black for the EI and EI$_R$ (**e**) and PI (**f**) deployments. The EI (blue star)/EI$_R$ (red star) and PI simulations (blue star) are within 10 and 5 km of sediment trap trajectories, respectively. Dispersion simulations indicate that 99% of particles from the 50, 150 and 300 m traps originated in circles of radius 2, 5 and 7 km, respectively. **g**, TEP concentrations were low in the upper 50 m at EI and EI$_R$ and highest at LI, as determined by ANOVA. The letters above the boxes denote statistically different groups. Pairwise comparisons for EI:EI$_R$, EI:LI, EI:PI, EI$_R$:LI, EI$_R$:PI and LI:PI gave P values of 0.99, 0.01, 0.09, 0.08, 0.54 and 0.34, respectively. For EI, EI$_R$, LI and PI, $n = 12$, 3, 3 and 9 station replicates, respectively. Negative optical density measurements are not illustrated. **h**, SEM images from EI at 10 and 150 m, respectively, showed loose aggregates of cells and coccoliths compared with densely aggregated particles entrapped in a polysaccharide-like substance. The images are singular qualitative descriptors representative of ten images for 10 m and eight images for 150 m. In **c** and **g**, the box bounds denote 25 and 75% quantiles around the median (thick line), and vertical capped lines indicate the maximum and minimum data values. Outliers are indicated with a + sign. In **e** and **f**, the satellite overlay pixels are $n = 1$.

While we recognize that sinking oceanic particles can be complex and can derive from various sources, one mechanism that could induce vertical transport and export of infected cells is TEP-based particle aggregation. With a buoyant density of 0.70–0.84 g cm^{-3}, TEP can lead to 'ascending particles'[25] and enhance the retention of particulate carbon in the upper ocean. However, association with denser cellular material such as $CaCO_3$-containing coccoliths may form large, dense aggregates with higher sinking rates, as has been observed previously with dinoflagellate thecal plates, where sinking rates increased exponentially with aggregate size[26]. Laboratory-based experimental data indeed demonstrated a mechanistic connection between viral infection and TEP production and aggregation,

whereby enhanced TEP production and aggregate formation was observed during the early phase of EhV infection of a calcified *E. huxleyi* strain, before cell lysis (Supplementary Fig. 12). Mixed-layer TEP concentrations were significantly higher for LI compared with EI populations, corroborating previous studies showing TEP accumulation as characteristic of the late stages of infection[7] (Fig. 4g). While in situ TEP concentrations were low at EI and EI_R, deck-board bottle incubations of these infected populations revealed enhanced TEP production over a three-day period (Supplementary Table 3), suggesting that in the absence of export these populations were producing elevated TEP. In situ, large (>200 µm), densely packed aggregates of coccoliths and calcified cells enveloped in a polysaccharide-like film were observed for EI at 150 m with scanning electron microscopy (SEM), while looser aggregates dominated the particle field for samples obtained at shallower depths in the mixed layer (upper ~20 m) (Fig. 4h). Taken together, these data support the notion that EhV infection of EI populations led to enhanced TEP production and larger particle aggregation, thereby facilitating sinking and carbon export. In contrast, the LI and PI stations were characterized by material that remained in the mixed layer. Late-stage TEP accumulation may be due to limited ballasting from remaining liths and calcified cells. We acknowledge that other cohabitating algae may have also contributed TEP in these blooms[26], but our data collectively suggest that infected *E. huxleyi* cells were a strong contributor at EI and EI_R.

The coupling of infection with grazing and faecal pellet production may have concurrently contributed to the particle composition and enhanced export fluxes observed at EI and EI_R. High *E. huxleyi*-specific microzooplankton grazing rates of 0.34 and 0.90 d^{-1} were measured for infected cell populations at EI and EI_R, respectively (Chl *a*-based grazing rates were 0.49 and 0.13 d^{-1}, respectively; Supplementary Fig. 13), indicating that grazing was indeed an important contributor to *E. huxleyi* mortality in the upper mixed layer, with comparable rates to previous studies in the North Atlantic[27]. Ecosystem interactions between grazing and infection are yet unresolved, as infection can manifest in enhanced[18] or deterred grazing[28]. The aforementioned infection-induced aggregation would serve to increase the accessibility of small *E. huxleyi* cells (5 µm) to grazing by large macrozooplankton[17] and further facilitate flux through faecal pellet production with sinking rates of >100 m d^{-1} (ref. [29]). Taken together with our previous observations of infected *E. huxleyi* cells (via EhV-derived MCP genes) within the gut content of >80% of copepods examined at EI and PI[20], these findings are supportive of intense grazing on, and preferential export of, infected cells by both micro- and macrozooplankton during NA-VICE. To date, this interactive coupling between infection and grazing ecosystem pathways and their collaborative impact on carbon export has been largely unexplored, as they have traditionally been seen as distinct mortality and removal mechanisms.

We found no evidence that nutrient limitation was a contributing factor to mortality, TEP production, aggregation or enhanced export at these stations. Nutrient additions (N, P and Si at 6.0, 0.38 and 6.0 µM, respectively) to microzooplankton dilution experiments yielded statistically indistinguishable changes in cell abundance relative to non-nutrient addition incubations (Supplementary Fig. 13). We also found only very weak relationships between the photochemical quantum yield of PSII (F_v/F_m) and nutrient concentrations (Supplementary Fig. 14), arguing against any significant impact of nutrient stress on photophysiology.

Our findings provide multilayered evidence that active *Coccolithovirus* infection of *E. huxleyi* stimulates coupled TEP production, particle aggregation and high zooplankton grazing within mesoscale open-ocean blooms in the North Atlantic and greater downward vertical fluxes and carbon export. The integration of our biomolecular in situ optics and satellite hindcasting uniquely contextualized these findings across three distinct bloom snapshots (with separate Chl and PIC histories) and layered them into a conceptual model of an entire *E. huxleyi* bloom and EhV-induced bust cycle from early June to mid-July 2012 (ref. [8]) (Fig. 4 and Supplementary Figs. 5 and 15). The viral shunt observed in bacterioplankton and phytoplankton systems[2] provides a conduit whereby carbon is remineralized in the surface ocean, but infection of ballasted, biomineral-containing phytoplankton (such as *E. huxleyi*) appears to stimulate vertical export flux, an idea consistent with recent observations that variability in carbon export to 150 m is best explained by viral gene abundance[30]. The widespread distribution of *E. huxleyi* and the fact that investigations regularly find EhV production associated with mesoscale bloom termination across the North Atlantic serves as an important temporal and spatial context for our findings. Notably, similar investigations have yet to be performed in the Pacific Ocean and Southern Ocean calcite belt, where large-scale *E. huxleyi* blooms occur. While the relative contributions of transport mechanism(s)—via the sinking of TEP-induced aggregates and/or a coupling with grazing and packaging of infected cells in faecal pellets—remain unresolved, our results highlight virus infection as a pervasive ecosystem process that can facilitate export fluxes into the mesopelagic and enhance biological pump efficiency. Our work reveals layers of carbon flux biogeochemistry the quantitative contributions of which will help in the decades-long challenge of resolving ecosystem influences on carbon export.

Methods

North Atlantic field sampling. The NA-VICE (cruise KN207-03; 13 June to 16 July 2012) traversed a ~2,000 nautical mile transect from Ponta Delgada, Azores to Reykjavik, Iceland aboard the *RV Knorr*, during which time water and sediment samples were collected at 30 discrete station locations (see http://www.bco-dmo.org/project/2136). Water was collected using 10 l Niskin bottles mounted on a 24-position rosette equipped with a Seabird SBE CTD profiler. Water from each of six depths (mostly within the upper mixed layer and extending down to 150 m) was filtered onto various membrane filters to collect host cell biomass and associated viruses for lipid and nucleic acid analyses (see below for details). All filters were snap-frozen in liquid nitrogen and stored at −80 °C until processed. Analytical flow cytometry of water collected during the CTD casts was used to enumerate both *E. huxleyi* cells and EhVs, as well as to perform diagnostic staining analyses (see below for details). Surface-tethered net and cylindrical sediment traps were simultaneously deployed (50, 150 and 300 m). An autonomous optical profiler was deployed and programmed to sample to a depth of 300 m (see below for details).

This study focused on three four-day process stations (EI, EI_R and PI) conducted during the cruise where Lagrangian sampling methods were employed. EI was re-occupied for four days as EI_R. The ship tracked coherent water features by maintaining its position with deployed, drifting sediment traps. Profiling floats were also deployed for the duration of each Lagrangian observation. The fourth location (LI) was visited for one day with multiple CTD casts, as well as the deployment of an optical profiling float that profiled the feature for five days. LI was sampled over 6 d using the optical profiling float. CTD cast measurements and water samples were taken at deployment and recovery, and remote-sensing imagery was taken from year days 150–200 (ref. [8]). Measurements of LI were complemented by month-long satellite observations of the bloom, observing the entire bloom cycle from initiation to termination[8]. Ship-based sampling was also conducted when the vessel returned to LI to recover the float, but with overboard hose pumped sampling due to a damaged CTD rosette at the end of the cruise.

Satellite remote sensing. We used the 1 km resolution level 2 Moderate Resolution Imaging Spectroradiometer (MODIS) onboard the Aqua satellite (MODIS/Aqua) to obtain ocean colour imagery data of PIC, near-surface Chl *a*, remote-sensing reflectance centred at 555 nm (Rrs 555) and remote-sensing reflectance centred at 547 nm (Rrs 547), which were downloaded daily from the National Aeronautics and Space Administration (NASA) Ocean Color Web (https://oceancolor.gsfc.nasa.gov/) and further processed (geographically resampled, reprojected over the target areas and statistically analysed) aboard *RV Knorr* using SeaDAS version 6.x software (https://seadas.gsfc.nasa.gov/). The standard operational algorithms included as part of the standard level 2 and level 3 OC suite products provided by NASA for each of the geophysical parameters were used (https://modis.gsfc.nasa.gov/data/dataprod/). The main aim was to locate *E. huxleyi* populations based on the available satellite information. These also included daily AVISO altimetry maps (http://www.aviso.altimetry.fr) with information on mean geostrophic currents. Areas of research included ocean cyclonic (upwelling in the centre, high satellite-derived Chl *a* concentrations initially, low satellite-derived PIC, low Rrs 555 and low Rrs 547) and anticyclonic (downwelling in the centre, low satellite-derived

Chl *a* concentrations initially, high satellite-derived PIC, high Rrs 555 and high Rrs 547) structures in the water.

In situ optical profiling. Two profiling floats equipped with Bio-Optical Sensor System mini (float numbers 8493 and 8502; Satlantic) were used on multiple deployment operations during the cruise and recovered after leaving each station. Floats were deployed at each of the process stations and programmed to profile from 300 m to the surface; the actual profiling depth varied from 200–300 m. Deployments lasted between 91 and 123 h with ~4 h profile cycles and ~2.5 m vertical resolution. Deployments were accompanied by shipboard sampling and sediment traps along the Lagrangian path, except at LI where the deployment was only anchored by ship sampling at the beginning and end of the deployment. Floats were equipped with an ECO Triplet puck (to measure Chl fluorescence, B_b (700 nm) and CDOM), Seapoint turbidity meter, oxygen optode (AADI), multispectral radiometer (to measure photosynthetically active radiation (PAR), downward irradiance (E_d; 412, 443 and 490 nm)) and CTD.

Fluorescence data were calibrated to ship-based Chl *a* measurements using nighttime float profiles (between 23:00 and 04:00 h) and adjacent CTD casts ($\mu g l^{-1}$). Daytime profiles exhibited significant non-photochemical quenching (NPQ) in the upper water column, which reduces the observed Chl *a* measurements. To account for observed NPQ, fluorescence and E_d (443 nm) data from the top 20 m were binned in 5 m intervals for individual profiles. Binned fluorescence data were interpolated between night casts for predicted day-cast fluorescence values in the absence of NPQ. The ratio of measured day-cast fluorescence to predicted day-cast fluorescence was fit in a two-term exponential model against E_d (443 nm). Individual fluorescence data were NPQ corrected using the E_d (443 nm) measurement from the associated data burst.

B_b was initially calibrated according to manufacturer's instructions. Dark offsets for B_b were then accounted for by subtracting the lowest value observed during individual deployments from the data. B_b transformation into the spike signal was performed in accordance with ref. [19]. The spike transformation removes the background signal by running minimum and maximum filters along profiles, leaving only the anomalously high spikes in the signal. Similar B_b spikes have been interpreted as aggregated phytoplankton and detrital matter in the North Atlantic following an intense bloom[19]. B_b spikes were averaged in 10 m, 12 h bins. Spike changes over time were negligible so bins were modified to include all data at 10 m depth intervals over the duration of the deployments. Standard error around the mean of these bins was calculated from the individual data values within the bin, which conservatively contained at least 50 values.

Salinity and temperature corrections for dissolved oxygen were provided by the sensor operation manual. Dissolved oxygen percent saturation was calculated with SW_SAT02 MATLAB script (http://www.marine.csiro.au/~morgan/seawater). Oxygen use measurements were performed using similar methods to ref. [31]. Data were separated into 10 m depth bins between 50 and 250 m before calculating the linear slope of oxygen concentration versus time over the deployment periods. Oxygen use was converted to carbon remineralization (C_{remin}) using the ratio organic carbon (C_{org}):O_2 = 0.688 (ref. [32]). Data above 50 m were excluded; this depth conservatively represented the bottom of the euphotic zone and was well below the mixed layer depth at each station (Supplementary Fig. 6). PI was excluded from the C_{remin} analysis because of float movement and mixing into another water mass, which influenced the change in dissolved oxygen, as observed by an abrupt change in depth horizon salinity >0.01 ppt over the deployment. It was assumed that oxygen production and diffusion had a negligible influence on this analysis based on the constraints implemented and the relatively short timescales over which the analysis was performed. For comparison, C_{remin} was also determined along isopycnals to examine the possible influences of internal waves; this approach yielded similar results to our depth-binned analysis (not shown).

CDOM measurements from the two floats were calibrated to each other by subtracting the difference between the floats' average measurements between 100 and 150 m when both floats were profiling the EI eddy. Average CDOM measurements were calculated for each profile between the pycnocline, identified as the depth interval with the greatest change in density, and 100 m over the duration of deployments to identify changes in CDOM concentration over time. CDOM accumulation rate profiles were achieved similar to the oxygen utilization measurements, separating data into 10 m depth bins for the deployment period before calculating the linear slope of CDOM concentration versus time.

Sediment trap deployments. Vertically sinking, particulate carbon fluxes were measured at 50, 150 and 300 m according to ref. [22] and using surface-tethered cylindrical sediment traps (0.0125 m^2 cross-sectional area; materials and construction as described in ref. [33]). A mooring consisting of four traps at each depth, a surface buoy, a wave-action mitigation bungee cord and several floats was deployed at each process station and allowed to drift for three to five days. The quasi-Lagrangian behaviour of the mooring during each deployment was confirmed by comparison of positional data obtained from an Argos satellite beacon mounted on the surface buoy with shipboard ADCP data from the *RV Knorr*, which trailed the mooring at a range of one to two nautical miles. Traps were prepared, deployed and recovered as described in ref. [33]. Traps were then sampled for particulate carbon in accordance with ref. [33], except that the screened brine suspension (350 µm pore size to exclude macrozooplankton) was filtered onto a series of precombusted, 47 mm GF/F filters (0.7 µm nominal pore size). Field and analytical blanks were collected at each station. Filters were immediately frozen in liquid nitrogen and then stored at −80 °C. Analysis of POC and PIC in the frozen samples was as described in ref. [22].

Particulate material was also collected for biomolecular and microscopic analysis from the appropriate depth using a series of surface-tethered, large-diameter net traps with a detachable 0.2 µm mesh cod end[34], also at 50, 150 and 300 m. These traps were allowed to drift with a surface mooring for approximately 24 h in the same eddy feature as the corresponding cylindrical sediment traps. The exact deployment time was controlled using a remote acoustic release, which allowed us to close the traps before recovery. Upon recovery, the particle material in the cod end was homogenized by gentle shaking, then quantitatively split into fractions using an eight-way rotating electric splitter[35]; aliquots were taken from one or more of these fractions, screened to 350 µm to exclude macrozooplankton and dispensed quantitatively into replicate BOD bottles for incubation.

Lipid analysis. Total lipid extracts were extracted from frozen biomass collected onto 0.2 µm pore-size Durapore membrane filters (GVWP-type; Millipore) using a modified Bligh and Dyer extraction procedure[36,37]. An internal standard of 2,4-dinitrophenylmodified phosphatidylethanolamine was added during extraction. Total lipid extracts were analysed by normal-phase high-performance liquid chromatography (HPLC) tandem mass spectrometry (MS^2) using an Agilent 1200 HPLC coupled to a Thermo Scientific TSQ Vantage Triple-Stage Quadrupole Mass Spectrometer. Chromatography and mass spectrometry conditions were as described in ref. [37]. Characteristic retention time and MS^2 fragmentation spectra were used to identify lipid classes, which were then quantified by peak area for a given MS^2 mass chromatogram as in previous studies[7,13].

For sGSL, hGSL and vGSL, instrument response was accounted for by comparison with external standard response factor calibrations acquired from a dilution series of a soy glucocerebroside (Avanti Polar Lipids) standard run immediately before analysis[14].

Deviations from previously published methodology[7,13] were as follows.

For vGSL, the selected reaction monitoring (SRM) mode was used for the 734.7 to 572.7 transition, representing the environmental vGSL lipid species as identified in ref. [10]. This SRM was used instead of the neutral loss or precursor ion scanning modes applied in previous investigations[13,14] due to its greater sensitivity and the low abundance of target species. The vGSL SRM data were then corrected for instrument response based on a calibration curve from the 714.7 to 534.7 SRM transition, which represents the predominant component of the soy glucocerebroside standard. These transitions represent the neutral loss of 162 Da, corresponding to a characteristic cleavage of the glycoside bond[10].

Host hGSL was characterized based on its characteristic long chain base-derived fragment of 257 Da and diagnostic retention time[7]. Two chromatographic peaks in the retention time window were observed in the MS^2 mass chromatogram for a precursor ion scan of 257 Da (P257). The first eluted at 10 min in line with hGSL in cultured *E. huxleyi*[14]; the second eluted at 12 min, co-eluting with vGSL[10,14]. The 10 min pure hGSL peak was cross-calibrated with its counterpart in the MS^2 mass chromatogram of a neutral loss of 180 Da (NL180). This response factor was used to quantify the hGSL in the 12 min peak by converting the unambiguous observed P257 peak to the equivalent value in NL180. The NL180 equivalent could then be quantified relative to the standard response factor (unavailable for the P257 mass chromatograms as the standard does not undergo this fragmentation). All quantities were corrected for recovery based on the 2,4-dinitrophenylmodified phosphatidylethanolamine internal standard. BLL species were quantified in terms of relative abundance and are presented as an internally normalized ratio[14].

Filtration, DNA extraction and subsequent quantitative PCR analysis. Water was first prefiltered through a 200 µm mesh to eliminate large macrozooplankton. Cell biomass (and associated viruses) was then collected from ~3–5 l of seawater by filtration onto large (142 mm diameter; 0.8 µm pore-size) PC filters (Millipore) to minimize clogging of the pores and the collection of extracellular viruses. The filters were immediately submerged in 10 ml extraction buffer (100 mM Tris-HCl pH 8, 250 mM EDTA pH 8, 100 mM NaCl and 1 vol% SDS) and homogenized at maximum speed on a Vortex-Genie (Mo Bio) for 10 min in the presence of 2 ml molecular-grade zirconium beads (equal amount of 100 µm and 400 µm diameter beads; OPS Diagnostics). The homogenized filters were subject to three freeze–thaw cycles by being submerged in liquid nitrogen, thawed in a water bath set to 50 °C and homogenized for 5 min at maximum speed using the Vortex-Genie. They were then stored at −80 °C until further DNA extraction and purification steps. Back in the laboratory, the homogenized filters in extraction buffer were thawed and 5 ml buffer was incubated for 1 h at 50 °C in the presence of 100 µg Proteinase K, followed by standard phenol/chlorophorm/isoamylalcohol 25:24:1 v/v extraction. Nucleic acids were precipitated with two volumes of 100% ethanol in the presence of 0.2 M NaCl. Following centrifugation for 20 min at 10,000 rcf, salts were removed by washing the DNA pellet with 20 ml of 70% ethanol. Upon centrifugation for 10 min at 10,000 rcf and removal of traces of ethanol, the DNA pellets were dissolved in 1× Tris-EDTA buffer (pH 8). Traces of impurities that

could inhibit enzymatic amplification reactions (PCR) were removed using the DNeasy PowerClean Cleanup Kit (Mo Bio).

E. huxleyi and EhV genetic markers (COI versus MCP) in the filtered particulate organic matter (POM) were quantified by SYBR Green-based qPCR assays using the primers and PCR conditions in ref. [38]. Using the same DNA extraction method, genomic DNA was extracted from a known number of *E. huxleyi* cells (strain 1516) and EhV particles (strain 86), as counted by fluorescence staining and analytical flow cytometry 15. To calibrate the COI- and MCP-specific qPCRs, tenfold dilution standard series of this genomic DNA were subjected to qPCR alongside the samples.

Photophysiology. The photochemical quantum yield (F_v/F_m) of natural populations was measured using a fluorescence induction and relaxation instrument (Satlantic). Discrete samples were collected from Niskin bottles and measured on the fluorescence induction and relaxation instrument immediately after a 10 min dark adaption[39]. Instrument settings in FireView 1.0.0 were as follows: gain, 2,400; samples, 10; sample delay, 1,000 ms; and PAR, 0. Analysis in FirePro 1.3.3 was completed with 240 iterations. Because samples were collected at different times of day, we acknowledge that the results may be biased by diel periodicity of fluorescence quenching.

Staining and flow cytometry. Phytoplankton cell abundance and diagnostic staining were performed using a Guava flow cytometer (Millipore). After water collection, samples were immediately prepared for analysis in duplicates. The instrument was set at a medium flow rate (0.59 µl s^{-1}). Triggering was set to collect all events above a Chl fluorescence (692 nm) threshold value of 1, with minimum gain for all detectors except yellow fluorescence, set at 23.63 nm. Samples were analysed using GuavaSoft InCyte 2.2.2. *Synechococcus* was gaited using red (threshold immediately above noise) and yellow fluorescence (threshold at 2×10^1 relative fluorescence units (RFU)) with an oblique gate that encompassed the range of the population. Low-fluorescence eukaryotes were gaited between red fluorescence (2×10^0 and 1×10^2 RFU) and side-scatter events above the axis, excluding events gaited as *Synechococcus*. High-fluorescence eukaryotes were gaited from red fluorescence (1×10^2 and above), as well as forward-scatter events above the axis, excluding the *E. huxleyi* population.

Populations of *E. huxleyi* were identified by forward scatter, side scatter and Chl fluorescence (692 nm) readings using gates based on the properties of cultured strains. *E. huxleyi* were enumerated by first gating events between 4×10^1–5×10^2 forward scatter and 5×10^2–1×10^4 side scatter, with the elevated side scatter from attached coccoliths being the primary characteristic separating this population from other high-fluorescence eukaryotes. A second gate was placed setting a minimum red fluorescence threshold at 1×10^2 RFU.

For live/dead cell analysis, samples were stained with 5 µM SYTOX Green (1:1000 dilution of stock) in the dark for 10 min. The green fluorescence (520 nm) threshold for SYTOX-positive cells was set at 10 RFU, based on the lower boundary of fluorescence for positive control, heat-treated samples. The average of the percent positive cells at each station, excluding samples collected at 150 m, was determined for each water mass.

Float optics and phytoplankton abundance correlations. B_b and Chl:B_b flow cytometry correlations were conducted using CTD casts and float profiles where the ship and float were within 2 km of each other during sampling and profiling. Correlated B_b and Chl:B_b values were an average of the three data points in the float profile with depths closest to the correlated CTD measurements sampling depth compared with in the scatter plot. Phytoplankton were gaited according to the following criteria: the *E. huxleyi* population was separated from other phytoplankton in a distinct event cluster based on forward scatter and high side scatter and separated from non-fluorescent particles with a minimum Chl fluorescence threshold. High-fluorescence eukaryotes included all events above a Chl fluorescence threshold of 100 RFU, where there was commonly a clear separation between high- and low-fluorescence populations. *Synechococcus* was gaited based on elevated fluorescence at 585, indicating the presence of phycoerythrin. Low-fluorescence eukaryotes had a Chl fluorescence below 100 RFU.

Grazing dilution experiments. We used a modified version of the standard dilution technique[40] to evaluate phytoplankton cell loss due to microzooplankton grazing, where encounter rates of predator–prey are inversely proportional to the dilution rate. Two dilution experiments were performed in near-surface waters characterized by *E. huxleyi* populations in the EI and EI_R stages (2 and 11 July 2017). Seawater was collected from approximately 10 m and a portion was passed through a 0.45 µm pore-size filter (Pall). Filtered diluent was added to each dilution bottle, which was then filled with whole seawater for final dilutions of 25, 50, 75 or 100% natural seawater. The natural seawater additions for the incubations were prescreened through a 200 µm Nitex mesh to remove large macrozooplankton grazers (for example, copepods). Aqueous macronutrients (N, P and Si) were added to all 2.7 l polycarbonate dilution bottles at levels of approximately 6, 0.38 and 6 µM, respectively. The bottles were incubated at approximately 40% surface irradiance at sea surface temperature for approximately 24 h. Chl-specific growth rates were calculated relative to the initial Chl values at time zero. Flow-cytometry-based cell counts were used to calculate cell-specific growth rates for comparison, as well as *E. huxleyi*-specific growth rates, similar to ref. [41].

Microscopy. SEM images of coccolithophores and particle aggregates were taken with a Phenom ProX desktop scanning electron microscope. Samples were collected on 0.4 µm pore-size Isopore filters and immediately desiccated with silica gel until visualization on SEM. Filters were quartered then loaded directly to a specimen mount for imaging. Images were taken at 1,300× and 2,200× magnification with 2,048×2,176 resolution, 10 kV and 6 s exposure. For coccolith counts, concentrations were calculated using the average coccolith count per image field of view and accounting for the volume filtered, field of view and filtration area.

Nutrient analysis. Seawater was filtered through precombusted GF/F filters and filtrate was stored at −80 °C in acid-washed Falcon tubes until analysis. Analyses of orthophosphate, total inorganic nitrogen (separating nitrate/nitrite and ammonia) and silicate were performed on thawed samples at the Rutgers' Nutrient Analysis Facility in the Department of Environmental Sciences (http://nutrientlab.rutgers.edu/) using standard facility protocols and a Lachat QuickChem 8500 Flow Injection Analysis System Nutrient Analyzer (Lachat Instruments). Concentrations were determined using the manufacturer's methods and facility standard operating protocols (ftp://boardwalk.marine.rutgers.edu/bidle/Protocols/). Detection limits for $NO_{2/3}$, NH_4 and P were 0.1 µM.

Pigment analysis. Standard Chl *a* extraction and fluorescence protocols were followed. Triplicate aliquots of 280 ml were filtered through 25 mm GF/F filters and extracted in 90% acetone for 24 h at −20 °C. The filtrate was then analysed on a 10AU fluorometer (Turner Designs) that had been calibrated with pure Chl *a* (Sigma Chemicals) using the non-acidification technique[42]. Water samples (2–4 l) were also collected from CTD casts and filtered onto 25 mm Whatman GF/F glass fibre filters and stored in liquid nitrogen until onshore analysis. Following extraction in 90% acetone, the samples were analysed on an Agilent 1100 HPLC system with diode array and fluorescence detection. The elution gradient used was a modified version of the method by ref. [43]. The exact elution gradient and protocols have been described in detail elsewhere[44]. The HPLC pigment concentrations were then analysed using the iterative matrix factorization programme CHEMTAX[45]. Output values of percent contribution phytoplankton taxa to Chl *a* were averaged for each of the four stations. Averages represent samples collected between 0 and 50 m.

TEP and protein analysis of field samples. Seawater was filtered onto a 0.4 µm pore-size Durapore filter and stained with 1 ml 0.02% Alcian Blue before freezing at −20 °C. For analysis, filters were soaked for 2 h in 2 ml of 80% sulphuric acid before removing the filter and measuring the optical density (787 nm) of extracted solution in a 1 cm cuvette on an Agilent 8453 spectrophotometer. Optical densities were calculated using the volume filtered for individual samples. Blank measurements were prepared with 0.2 µm-filtered seawater.

Protein concentration was measured on biomass from a known volume of filtered seawater (collected onto 0.8 µm pore-size filters; Millipore RAWG04700), which had been kept frozen at −80 °C until the time of analysis. Biomass was scraped from each filter into lithium dodecyl sulphate lysis buffer (140 mM Tris base, 105 mM Tris-HCl, 0.5 mM EDTA, 2% lithium dodecyl sulphate, 10% glycerol) with protease inhibitor cocktail (P2714; Sigma), frozen in liquid nitrogen and sonicated three times (Misonix; power setting of 2–3), followed by centrifuging (10,000 *g*, 10 min, 4°C). The supernatant was transferred to a fresh tube and the protein concentration was quantified using a BioRad DC Protein Assay Kit (BioRad 5000111), following the manufacturer's protocol. In brief, 25 µl of proprietary reagent A was mixed with 5 µl of each sample in duplicate within microtiter plate wells followed by the addition of 200 µl proprietary reagent B. Optical density at 750 nm was read on a microtiter plate reader (SpectraMax M3; Molecular Devices) after 15 min of incubation at 37 °C. Known concentrations of bovine serum albumin were used as standards.

Host–virus abundances and TEP analysis in laboratory-based experiments. Experiments used *E. huxleyi* strain DHB607 in triplicate in f/2-Si media. *E. huxleyi* virus 99B1 (ref. [46]) was added to exponentially growing cultures at a virus-to-host ratio of 5:1, based on the total number of virus-like particles as detected by flow cytometry in a primary EhV lysate stock. Virus-free controls were set by adding appropriate f/2-Si volume into exponentially growing cultures. Cultures were monitored daily for host and virus abundances, bulk TEP production and particle aggregation over a four-day period.

The total numbers of virus-like particles throughout the infection experiments were counted using SYBR Gold stain and an Influx Mariner 209S flow cytometer based on the protocol developed by ref. [47]. Briefly, a 1 ml subsample of each virus stock or infected culture was fixed with glutaraldehyde (final concentration of 0.5%), incubated in the dark at 4 °C for 15–30 min, snap-frozen in liquid nitrogen and stored at −80 °C until processed. Samples were thawed at room temperature and diluted 50-fold in Tris-EDTA buffer (1 M Tris pH 8, 0.5 M EDTA, Milli-Q) in 3 ml flow cytometery tubes. SYBR Gold was diluted into the Tris-EDTA buffer at a 20,000:1 ratio of the commercial stock. The subsamples were agitated and

incubated at 80°C for 10 min, followed by 5 min at room temperature in the dark. Each sample was analysed for 1 min on the influx at a variable flow rate measured in µl min^{-1}. The flow rate was adjusted for each set of measurements. Host cell abundance measurements were performed using an Accuri C6 flow cytometer (BD Biosciences), where 200 µl of the thawed samples was distributed into 96-well plates and the cells were counted using Chl red fluorescence (692 nm) versus side scatter.

TEP samples for optical density quantification with AB stain were prepared as described above with the following exceptions: 3 ml of each experimental treatment was filtered daily in triplicates and stained with 500 µl AB. The optical density (787 nm) of the AB-stained TEP was measured on a Molecular Devices SpectraMax M3 plate reader with optical density values corrected for f/2-Si media blanks and plotted against a xanthum gum standard curve of known concentrations.

TEP particles (including the particle size spectrum) associated with infected and virus-free cells were also visualized and characterized daily using FlowCam VisualSpreadsheet software (version 4.0.27; http://www.fluidimaging.com/products/particle-analysis-software). Before visualization, subsamples (500 µl) were stained with 200 µl of 0.02% AB and 20 µl of acetic acid at room temperature for 10 min and applied to the FlowCam sample intake. A 10× objective lens was used in the instrument's auto-image mode setting (20–30 frames per second) with the threshold set to image particles that ranged from 7–100 µm with a minimum distance between particles of 1 µm. The collection of particle images was restricted to those above 7 µm in diameter based on the known size range of *E. huxleyi* cells (that is, 3–8 µm) and an upper size cutoff of 100 µm based on the limitations of the size of the flow cell used. The flow rate was adjusted to 0.08–0.1 ml min^{-1} to prevent duplicate images and the auto-image mode was set to stop after imaging 100 µl volume. Files were analysed manually for quality control and identification of duplicate images. Particles were arbitrarily 'binned' into 12 particle size groups that spanned 5 µm in diameter (that is, 7–11, 12–16, 17–21, 22–26, 27–31, 32–36, 37–41, 42–46, 47–51, 52–56, 57–61 and 62–66 µm). The particles were sorted based on the average blue-to-green ratio of each image and their area-based diameter—a FlowCam image analysis setting that calculates the particle diameter based on the measured area of the visualized particle.

Measurements of PIC and POC. Particulate matter from 0.5–2 l of seawater was filtered in duplicate onto precombusted GF/F filters under light vacuum and snap-frozen in liquid nitrogen. Filters were placed into numbered, etched glass petri dishes and baked at 60 °C for drying. One filter designated for POC from each set was placed into a glass desiccator with concentrated HCl fumes for 24 h to dissolve PIC. The other filter was untreated and represented total carbon. All filters were trimmed, packed into tin boats and combusted in a NA 1500 CNS Analyzer (Carlo Erba). PIC was determined by taking the difference between total carbon and acidified POC sample. Due to instrument failure, two samples were excluded from the analysis. For resolution of *E. huxleyi* DHB607 culture PIC quotas, exponentially growing cells ('5×10^5 cells ml^{-1}) were filtered onto triplicate GF/F filters and prepared for POC and PIC analysis as above.

General statistics. Differences among stations were determined with one-way analysis of variance (ANOVA) in the MATLAB Statistics Toolbox for the following datasets: GSL inventories and ratios, MCP and COI gene copy number, TEP optical density, *E. huxleyi* cell inventories, percent live/dead *E. huxleyi*, dissolved nutrients, PIC and coccoliths. BLL lipid data were non-normal and therefore a Kruskal–Wallis test was applied. For all boxplots, outliers were greater than ±2.7 s.d. from the mean.

Sediment trap particle origins. As the sampling of sediment traps is dependent on both vertical and horizontal physical processes, it is useful to simulate the trajectories of particles captured in sediment traps[48] to determine whether particles originated in the region of interest, as opposed to adjacent water masses with differing biological processes. To simulate particle trajectories, we solve the following system of equations:

$$d(\overrightarrow{X}(t)+\overrightarrow{X}'(t))/dt=\overrightarrow{u}(t)+\overrightarrow{u}'(t) \quad (1)$$

where $\overrightarrow{X}$ is the low-frequency trajectory of a simulated particle, $\overrightarrow{X}'$ is the high-frequency trajectory associated with horizontal dispersion, $\overrightarrow{u}$ is the low-frequency water velocity and $\overrightarrow{u}'$ is the high-frequency velocity associated with dispersion. To solve these equations, we need to specify $\overrightarrow{u}(t)$, $\overrightarrow{u}'(t)$, and $\overrightarrow{X_i}=\overrightarrow{X}(t_i)$, where t_i is the initialization time.

The *RV Knorr* was equipped with a 75 kHz ADCP continuously measuring current profiles to approximately 600 m depth with 8 m resolution. The *RV Knorr* was often on station near the drifting sediment traps, providing sufficient current profile measurements to define the horizontal components of $\overrightarrow{u}(t)$ in most cases, the exception being EI_R (see below). The vertical component of $\overrightarrow{u}(t)$ is defined by the descent rate of particles that ultimately end up in the sediment trap. A value of 100 m d^{-1} was chosen to represent the average descent rate of particles[29,49].

There were no direct measurements of $\overrightarrow{u}'(t)$. The horizontal component was modelled as a probability distribution function (PDF; that is, a Gaussian distribution with a mean µ and s.d. σ). The $\overrightarrow{u}'(t)$ PDF was then used in a Monte Carlo simulation ($n=20{,}000$) to generate a set of trajectories representing the PDF of $\overrightarrow{X}'$ associated with dispersion. The mean (µ) is associated with the low-frequency velocities already obtained from ADCP data and thus assumed to be zero. The s.d. (σ) is associated with unresolved velocity scales and drifter motions not associated with the background velocity measured by the ADCP. We estimate this by comparing velocities measured by the ADCP and velocities derived from the drifting sediment traps. We assume the s.d. of this velocity difference to be σ, which is calculated to be ~20 cm s^{-1}. Note that this value includes any error in the ADCP measurements and the drifter locations so is an upper bound on σ, assuming these errors are uncorrelated with $\overrightarrow{u}(t)$, which is likely.

Since the objective was to determine the potential origin of particles in the sediment trap, it was desirable to define $\overrightarrow{X_i}$ and t_i as the location and time where traps were recovered for processing. We chose a representative trap recovery time, which allows sufficient ADCP data to perform the simulations. This was possible for EI and PI; however, EI_R is a shorter record with more gaps, so the $\overrightarrow{X_i}=\overrightarrow{X}(t_i)$ chosen allows for the longest simulation time. Initialization depths where 50, 150 and 300 m, representing the depths of the drifting sediment traps.

Three simulations were carried out for EI and PI—one for each initialization depth. Simulations were ended after 7.2, 31.2 and 64.8 h—the time it took for particles to reach 20 m depth (the depth corresponding to *E. huxleyi* maximum abundance) from 50, 150 and 300 m, respectively. The available ADCP data only allowed for 2 simulations during the EI_R time period—one each for the 50 and 150 m traps.

Life Sciences Reporting Summary. Further information on experimental design is available in the Life Sciences Reporting Summary.

Code availability. MATLAB scripts for the profiling floats, C_{remin}, spike signature analysis and particle origins, as well as for generating the satellite images, are available at ftp://boardwalk.marine.rutgers.edu/bidle/Datasets/Laber_EhuxEhV_NA-VICE/CodeInfo/.

Data availability. Data supporting the findings of this study are available within the paper and its Supplementary Information files. Flow cytometry source data (as.fcs files) and raw data on which the statistics were performed are accessible at ftp://boardwalk.marine.rutgers.edu/bidle/Datasets/Laber_EhuxEhV_NA-VICE/DataFiles/. Metadata for the NA-VICE cruise can be found at www.bco-dmo.org/project/2136. Datasets for the HPLC pigments, sediment trap flux and water column respiration rates are available at http://www.bco-dmo.org/deployment/58868. MATLAB scripts for the profiling floats, C_{remin}, spike signature analysis and particle origins, as well as for generating the satellite images, are available at ftp://boardwalk.marine.rutgers.edu/bidle/Datasets/Laber_EhuxEhV_NA-VICE/CodeInfo/.

Received: 11 December 2017; Accepted: 9 February 2018;
Published online: 12 March 2018

References

1. Field, C. B., Behrenfeld, M. J., Randerson, J. T. & Falkowski, P. Primary production of the biosphere: integrating terrestrial and oceanic components. *Science* **281**, 237–240 (1998).
2. Weitz, J. S. et al. A multitrophic model to quantify the effects of marine viruses on microbial food webs and ecosystem processes. *ISME J.* **9**, 1352 (2015).
3. Rousseaux, C. S. & Gregg, W. W. Interannual variation in phytoplankton primary production at a global scale. *Remote Sens.* **6**, 1–19 (2013).
4. Berelson, W. et al. Relating estimates of $CaCO_3$ production, export, and dissolution in the water column to measurements of $CaCO_3$ rain into sediment traps and dissolution on the sea floor: a revised global carbonate budget. *Global Biogeochem. Cycles* **21**, GB1024 (2007).
5. Tyrrell, T. & Merico, A. in *Coccolithophores* (eds Thierstein, H. R. & Young, J. R.) 75–97 (Springer, Berlin, 2004).
6. Bratbak, G., Egge, J. K. & Heldal, M. Viral mortality of the marine alga Emiliania huxleyi (Haptophyceae) and termination of algal blooms. *Mar. Ecol. Prog. Ser.* **93**, 39–48 (1993).
7. Vardi, A. et al. Host–virus dynamics and subcellular controls of cell fate in a natural coccolithophore population. *Proc. Natl Acad. Sci. USA* **109**, 19327–19332 (2012).
8. Lehahn, Y. et al. Decoupling physical from biological processes to assess the impact of viruses on a mesoscale algal bloom. *Curr. Biol.* **24**, 2041–2046 (2014).
9. Schatz, D. et al. Hijacking of an autophagy-like process is critical for the life cycle of a DNA virus infecting oceanic algal blooms. *New Phytol.* **204**, 854–863 (2014).
10. Vardi, A. et al. Viral glycosphingolipids induce lytic infection and cell death in marine phytoplankton. *Science* **326**, 861–865 (2009).
11. Bidle, K. D., Haramaty, L., e Ramos, J. B. & Falkowski, P. Viral activation and recruitment of metacaspases in the unicellular coccolithophore, *Emiliania huxleyi*. *Proc. Natl Acad. Sci. USA* **104**, 6049–6054 (2007).

12. Ziv, C. et al. Viral serine palmitoyltransferase induces metabolic switch in sphingolipid biosynthesis and is required for infection of a marine alga. *Proc. Natl Acad. Sci. USA* **113**, E1907–E1916 (2016).
13. Fulton, J. M. et al. Novel molecular determinants of viral susceptibility and resistance in the lipidome of *Emiliania huxleyi*. *Environ. Microbiol.* **16**, 1137–1149 (2014).
14. Hunter, J. E., Frada, M. J., Fredricks, H. F., Vardi, A. & Van Mooy, B. A. Targeted and untargeted lipidomics of *Emiliania huxleyi* viral infection and life cycle phases highlights molecular biomarkers of infection, susceptibility, and ploidy. *Front. Mar. Sci.* **2**, 81 (2015).
15. Bidle, K. D. The molecular ecophysiology of programmed cell death in marine phytoplankton. *Annu. Rev. Mar. Sci.* **7**, 341–375 (2015).
16. Castillo, C. R., Sarmento, H., Alvarez-Salgado, X. A., Gasol, J. M. & Marraséa, C. Production of chromophoric dissolved organic matter by marine phytoplankton. *Limnol. Oceanogr.* **55**, 446–454 (2010).
17. Passow, U. & Alldredge, A. L. Do transparent exopolymer particles (TEP) inhibit grazing by the euphausiid *Euphausia pacifica*? *J. Plankton Res.* **21**, 2203–2217 (1999).
18. Evans, C. & Wilson, W. H. Preferential grazing of *Oxyrrhis marina* on virus infected *Emiliania huxleyi*. *Limnol. Oceanogr.* **53**, 2035–2040 (2008).
19. Briggs, N. et al. High-resolution observations of aggregate flux during a sub-polar North Atlantic spring bloom. *Deep Sea Res. I Oceanogr. Res. Pap.* **58**, 1031–1039 (2011).
20. Frada, M. J. et al. Zooplankton may serve as transmission vectors for viruses infecting algal blooms in the ocean. *Curr. Biol.* **24**, 2592–2597 (2014).
21. Azam, F. Microbial control of oceanic carbon flux: the plot thickens. *Science* **280**, 694–696 (1998).
22. Collins, J. R. et al. The multiple fates of sinking particles in the North Atlantic Ocean. *Glob. Biogeochem. Cycles* **29**, 1471–1494 (2015).
23. Denman, K. & Gargett, A. Biological–physical interactions in the upper ocean: the role of vertical and small scale transport processes. *Annu. Rev. Fluid Mech.* **27**, 225–256 (1995).
24. Sheyn, U. et al. Expression profiling of host and virus during a coccolithophore bloom provides insights into the role of viral infection in promoting carbon export. *ISME J.* https://doi.org/10.1038/s41396-017-0004-x (2018).
25. Azetsu-Scott, K. & Passow, U. Ascending marine particles: significance of transparent exopolymer particles (TEP) in the upper ocean. *Limnol. Oceanogr.* **49**, 741–748 (2004).
26. Alldredge, A. L., Passow, U. & Haddock, H. The characteristics and transparent exopolymer particle (TEP) content of marine snow formed from thecate dinoflagellates. *J. Plankton Res.* **20**, 393–406 (1998).
27. Morison, F. & Menden-Deuer, S. Early spring phytoplankton dynamics in the subpolar North Atlantic: the influence of protistan herbivory. *Limnol. Oceanogr.* **60**, 1298–1313 (2015).
28. Vermont, A. et al. Virus infection of *Emiliania huxleyi* deters grazing by the copepod *Acartia tonsa*. *J. Plankton Res.* **38**, 1194–1205 (2016).
29. Harris, R. Zooplankton grazing on the coccolithophore *Emiliania huxleyi* and its role in inorganic carbon flux. *Mar. Biol.* **119**, 431–439 (1994).
30. Guidi, L. et al. Plankton networks driving carbon export in the oligotrophic ocean. *Nature* **532**, 465–470 (2016).
31. Martz, T. R., Johnson, K. S. & Riser, S. C. Ocean metabolism observed with oxygen sensors on profiling floats in the South Pacific. *Limnol. Oceanogr.* **53**, 2094–2111 (2008).
32. Anderson, L. A. & Sarmiento, J. L. Redfield ratios of remineralization determined by nutrient data analysis. *Glob. Biogeochem. Cycles* **8**, 65–80 (1994).
33. McDonnell, A. M. & Buesseler, K. O. A new method for the estimation of sinking particle fluxes from measurements of the particle size distribution, average sinking velocity, and carbon content. *Limnol. Oceanogr.* **10**, 329–346 (2012).
34. Peterson, M. L., Wakeham, S. G., Lee, C., Askea, M. A. & Miquel, J. C. Novel techniques for collection of sinking particles in the ocean and determining their settling rates. *Limnol. Oceanogr. Methods* **3**, 520–532 (2005).
35. Lamborg, C. et al. The flux of bio- and lithogenic material associated with sinking particles in the mesopelagic "twilight zone" of the northwest and North Central Pacific Ocean. *Deep Sea Res. II Top. Stud. Oceanogr.* **55**, 1540–1563 (2008).
36. Bligh, E. G. & Dyer, W. J. A rapid method of total lipid extraction and purification. *Can. J. Biochem. Physiol.* **37**, 911–917 (1959).
37. Popendorf, K. J., Fredricks, H. F. & Van Mooy, B. A. Molecular ion-independent quantification of polar glycerolipid classes in marine plankton using triple quadrupole MS. *Lipids* **48**, 185–195 (2013).
38. Coolen, M. J. L. 7000 years of *Emiliania huxleyi* viruses in the Black Sea. *Science* **333**, 451–452 (2011).
39. Kolber, Z. S., Prášil, O. & Falkowski, P. G. Measurements of variable chlorophyll fluorescence using fast repetition rate techniques: defining methodology and experimental protocols. *Biochim. Biophys. Acta* **1367**, 88–106 (1998).
40. Landry, M. & Hassett, R. Estimating the grazing impact of marine micro-zooplankton. *Mar. Biol.* **67**, 283–288 (1982).
41. Evans, C., Archer, S. D., Jacquet, S. & Wilson, W. H. Direct estimates of the contribution of viral lysis and microzooplankton grazing to the decline of a *Micromonas* spp. population. *Aquat. Microb. Ecol.* **30**, 207–219 (2003).
42. Welschmeyer, N. A. Fluorometric analysis of chlorophyll *a* in the presence of chlorophyll *b* and pheopigments. *Limnol. Oceanogr.* **39**, 1985–1992 (1994).
43. Zapata, M., Rodríguez, F. & Garrido, J. L. Separation of chlorophylls and carotenoids from marine phytoplankton: a new HPLC method using a reversed phase C_8 column and pyridine-containing mobile phases. *Mar. Ecol. Progress. Ser.* **195**, 29–45 (2000).
44. DiTullio, G. & Geesey, M. E. in *Encyclopedia of Environmental Microbiology* (ed. Bitton, G.) 2453–2470 (Wiley, New York, 2002).
45. Mackey, M., Mackey, D., Higgins, H. & Wright, S. CHEMTAX—a program for estimating class abundances from chemical markers: application to HPLC measurements of phytoplankton. *Mar. Ecol. Progress. Ser.* **144**, 265–283 (1996).
46. Nissimov, J. I. et al. Draft genome sequence of four coccolithoviruses: *Emiliania huxleyi* virus EhV-88, EhV-201, EhV-207, and EhV-208. *J. Virol.* **86**, 2896–2897 (2012).
47. Brussaard, C. P., Payet, J. P., Winter, C. & Weinbauer, M. G. Quantification of aquatic viruses by flow cytometry. *Man. Aquat. Viral Ecol.* **11**, 102–107 (2010).
48. Siegel, D. A., Fields, E. & Buesseler, K. O. A bottom-up view of the biological pump: modeling source funnels above ocean sediment traps. *Deep Sea Res. I Oceanogr. Res. Pap.* **55**, 108–127 (2008).
49. Ploug, H., Iversen, M. H., Koski, M. & Buitenhuis, E. T. Production, oxygen respiration rates, and sinking velocity of copepod fecal pellets: direct measurements of ballasting by opal and calcite. *Limnol. Oceanogr.* **53**, 469–476 (2008).

Acknowledgements

We thank the captain and crew of the *RV Knorr* for assistance and cooperation at sea, as well as Marine Facilities and Operations at the Woods Hole Oceanographic Institution for logistical support. We thank R. Fernandes and S. Prakya (University of the Azores) and I. Bashmachnikov (Saint Petersburg University) for daily downloading and sending MODIS and AVISO altimetry data to the *RV Knorr* for onboard processing. We also thank B. Edwards for logistical help with sediment trap deployments and recoveries. R. Stevens (College of Charleston) and A. Neeley (NASA) provided assistance with the dilution experiments and CHEMTAX analyses, respectively. This study was supported by grants from the National Science Foundation to K.D.B. (OCE-1061876, OCE-1537951 and OCE-1459200), M.J.L.C., G.R.D., A.V. and B.A.S.V.M. (OCE-1050995), and R.J.C. and E.J.H. (OCE-1325258), and from the Gordon and Betty Moore Foundation to K.D.B. (GBMF3789) and B.A.S.V.M. (GBMF3301).

Author contributions

C.P.L. operated the vertical profiling floats, processed the PIC, POC and nutrient samples, analysed and interpreted the bio-optical, lipid, genetic, flow cytometry, SEM, HPLC pigment, nutrient, F_v/F_m and TEP data, and wrote the manuscript. J.E.H. processed, analysed and interpreted the lipid samples and data, and provided extensive manuscript feedback. F.C. processed the MODIS/Aqua satellite data. J.R.C. helped with deployment and recovery of the sediment traps, analysed the sediment PIC and POC flux data, and provided extensive manuscript feedback. E.H. performed statistical particle funnel analyses and overlaid data onto the satellite imagery. B.M.S. processed, organized, and helped analyse the flow cytometry data, and also helped process nutrient samples. E.B. aided in vertical profile float mission planning, and processing and interpreting of the bio-optical data. K.M. performed qPCR for MCP and COI quantification. M.F. collected the SEM samples and provided extensive manuscript feedback. K.T. collected nutrient samples, analysed the F_v/F_m data and provided extensive manuscript feedback. C.M.B. collected and processed the flow cytometry samples. L.H. collected and processed the TEP samples, and organized the TEP and F_v/F_m data. J.O. led the operational deployment and recovery of the sediment traps. H.F. processed the GSL lipid data. U.S. collected and processed the flow cytometry data. J.I.N. designed the laboratory-based experiments and performed analyses of TEP production and particle dynamics. R.V. performed the laboratory-based experiments and helped with the analyses of TEP production and particle dynamics. Y.L. collected and processed the hindcast satellite data at the LI station. R.J.C. helped with analysis of the ADCP data, sediment trap trajectories and statistical particle funnel analysis. A.M.M. acquired, interpreted and processed the MODIS/Aqua Chl *a*, PIC, Rrs 555 and Rrs 547 data during the NA-VICE field campaign. M.J.L.C. was a co-investigator during the NA-VICE cruise, and collected and processed DNA samples for MCP and COI quantification. A.V. was a co-investigator during the NA-VICE cruise and collected nutrient samples. G.R.D. was a co-investigator during the NA-VICE cruise, collected and processed Chl *a* and HPLC pigment data, and analysed pigment data in CHEMTAX. B.A.S.V.M. was a co-investigator during the NA-VICE cruise, oversaw lipid analysis and sediment flux measurements, and provided extensive discussion and feedback throughout the

investigation and during manuscript preparation. K.D.B. obtained funding support for the work, was chief scientist on the NA-VICE cruise, aided in interpreting the results and provided intellectual guidance in all aspects of the study. All authors read and approved the final manuscript.

Competing interests

The authors declare no competing interests.

Additional information

Supplementary information is available for this paper at https://doi.org/10.1038/s41564-018-0128-4.

Correspondence and requests for materials should be addressed to K.D.B.

nature research

Corresponding author(s): Kay D. Bidle; bidle@marine.rutgers.edu

☐ Initial submission ☐ Revised version ☒ Final submission

Life Sciences Reporting Summary

Nature Research wishes to improve the reproducibility of the work that we publish. This form is intended for publication with all accepted life science papers and provides structure for consistency and transparency in reporting. Every life science submission will use this form; some list items might not apply to an individual manuscript, but all fields must be completed for clarity.

For further information on the points included in this form, see Reporting Life Sciences Research. For further information on Nature Research policies, including our data availability policy, see Authors & Referees and the Editorial Policy Checklist.

Experimental design

1. Sample size

Describe how sample size was determined.

Sampling of coccolithophore blooms in the North Atlantic was opportunistic and no previous knowledge of bloom state existed before sampling. Sampling at each station occurred in Lagranian mode over 4-6 days where time permitted. See manuscript text; Materials and Methods.

2. Data exclusions

Describe any data exclusions.

For oxygen utilization measurements, data within the euphotic, oxygen producing layer, were excluded from analysis. This criteria was pre-established.
Station PI was excluded from carbon remineralization estimates because of observed mixing water masses. Two samples were excluded from total carbon and particulate inorganic carbon samples due to instrument failure. See Materials and Methods for details of these exclusions.

3. Replication

Describe whether the experimental findings were reliably reproduced.

Given this largely a field-based study on natural phytoplankton populations in the North Atlantic, the majority of data reported is observational data. Some lab-based experimental findings are reported in Figure S12. These data derive from incubation experiments with biological triplicate measurements for which standard error is reported.

4. Randomization

Describe how samples/organisms/participants were allocated into experimental groups.

Water masses were targeted via satellite remote sensing with arbitrary location within water masses being selected for sampling. Lagrangian measurements occurred following occupation using float and sediment trap movement to center ship. See manuscript text and Materials and Methods for details.

5. Blinding

Describe whether the investigators were blinded to group allocation during data collection and/or analysis.

During expedition and sample processing/assessment, investigators were blind to bloom conditions during sampling. Generally, samples were numbered upon collection and during analysis there was no knowledge of sample location/depth. Because knowledge of biological dynamics was limited prior to data analysis, investigators were blind to environmental conditions during sampling.

Note: all studies involving animals and/or human research participants must disclose whether blinding and randomization were used.

6. Statistical parameters

For all figures and tables that use statistical methods, confirm that the following items are present in relevant figure legends (or in the Methods section if additional space is needed).

n/a	Confirmed
☐	☒ The exact sample size (*n*) for each experimental group/condition, given as a discrete number and unit of measurement (animals, litters, cultures, etc.)
☐	☒ A description of how samples were collected, noting whether measurements were taken from distinct samples or whether the same sample was measured repeatedly
☐	☒ A statement indicating how many times each experiment was replicated
☐	☒ The statistical test(s) used and whether they are one- or two-sided (note: only common tests should be described solely by name; more complex techniques should be described in the Methods section)
☐	☒ A description of any assumptions or corrections, such as an adjustment for multiple comparisons
☐	☒ The test results (e.g. *P* values) given as exact values whenever possible and with confidence intervals noted
☐	☒ A clear description of statistics including central tendency (e.g. median, mean) and variation (e.g. standard deviation, interquartile range)
☐	☒ Clearly defined error bars

See the web collection on statistics for biologists for further resources and guidance.

▸ Software

Policy information about availability of computer code

7. Software

Describe the software used to analyze the data in this study.	Software used to analyze data in this study included: Microsoft Excel, Matlab, and R.

For manuscripts utilizing custom algorithms or software that are central to the paper but not yet described in the published literature, software must be made available to editors and reviewers upon request. We strongly encourage code deposition in a community repository (e.g. GitHub). *Nature Methods* guidance for providing algorithms and software for publication provides further information on this topic.

▸ Materials and reagents

Policy information about availability of materials

8. Materials availability

Indicate whether there are restrictions on availability of unique materials or if these materials are only available for distribution by a for-profit company.	Given this largely a field-based study on natural phytoplankton populations in the North Atlantic, samples obtained are unique to this study and cannot be reproduced in laboratory experiments.

9. Antibodies

Describe the antibodies used and how they were validated for use in the system under study (i.e. assay and species).	N/A.

10. Eukaryotic cell lines

a. State the source of each eukaryotic cell line used.	N/A
b. Describe the method of cell line authentication used.	N/A
c. Report whether the cell lines were tested for mycoplasma contamination.	N/A
d. If any of the cell lines used are listed in the database of commonly misidentified cell lines maintained by ICLAC, provide a scientific rationale for their use.	N/A

▸ Animals and human research participants

Policy information about studies involving animals; when reporting animal research, follow the ARRIVE guidelines

11. Description of research animals

Provide details on animals and/or animal-derived materials used in the study.	N/A

Policy information about studies involving human research participants

12. Description of human research participants

Describe the covariate-relevant population characteristics of the human research participants.	N/A